PAPER

Electrical transport properties of TiO₂/MAPbI₃ and SnO₂/MAPbI₃ heterojunction interfaces under high pressure†

Yuqiang Li, [iD] *[ad] Yuhong Li,[ad] Qiang Zhang,[b] Xiaofeng Liu,[c] Yuanjing Li,[ad] Ningru Xiao,[e] Pingfan Ning,[d] Jingjing Wang,[ad] Jianxin Zhang[ad] and Hongwei Liu[ad]

The electrical transport properties of SnO₂(TiO₂)/MAPbI₃ (MA = CH₃NH₃⁺) heterojunction interfaces are investigated from ambient pressure to 20 GPa, and the transport properties are calculated by physical parameters such as trap energy density, binding energy, and charge transfer driving force and defect. Based on the partial density of states (PDOS) of the SnO₂/MAPbI₃ heterojunction interface MAI-termination and PbI₂-termination, greater charge transfer driving force and higher binding energy are observed, obviously showing the SnO₂-based heterojunction is more stable. The SnO₂/MAPbI₃ heterojunction interface possesses stronger electrical transport ability and is less prone to capture electrons compared with the TiO₂/MAPbI₃ heterojunction interface. The differential charge density spectrum shows that the density is lower in the trap energy level of SnO₂/MAPbI₃, whilst the effect of the charge transfer defect is weaker owing to the trap energy level only existing in SnO₂. The SnO₂/MAPbI₃ heterostructure interface is less prone to capture electrons. The greater electron concentration difference is attributed to oxygen vacancy (Vo₀) in the SnO-like environment, resulting in superior electron transport ability compared with the TiO-like environment.

1. Introduction

In the field of PSCs (perovskite solar cells), the interface problem is one of the key factors to determine efficiency and stability.[1–3] MAPbI₃ thin films can form heterojunction interfaces with TiO₂ or SnO₂, which will cause lattice distortion in the interface, affect electrical transport properties, and accelerate ion migration.[4–6] TiO₂ and SnO₂ respectively form electrical transport complexes O₂–Ti⁴⁺ and O₂–Sn⁴⁺.[7,8] SnO₂ is considered a substitute for TiO₂ due to its high electron mobility,[9] transmittance, and stability,[10–12] and less IV hysteresis. However, the band matching of SnO₂/MAPbI₃ is worse than that of TiO₂/MAPbI₃.[13,14] Generally, the comparative analysis of PSC efficiency for the SnO₂/MAPbI₃ and TiO₂/MAPbI₃ electron transport layers is complex.

Leijtens *et al.*[15] reported that oxygen adsorption instability acted on the electrical transport characteristics of the TiO₂/MAPbI₃ heterojunction surface under the excitation of ultraviolet light, because the holes on the valence band of TiO₂ recombine with the electrons at the oxygen adsorption point, resulting in the release of adsorbed oxygen molecules, forming a free electron and a positively charged oxygen vacancy on the conduction band. Yang *et al.*[16] reported a method of drastically improving solar cell efficiency by surface optimization of the TiO₂ electron transport layer (ETL) using a special ionic-liquid (IL), which shows high optical transparency and superior electron mobility. Shin *et al.*[17] found a low-temperature colloidal method for depositing La-doped BaSnO₃ films as a replacement for TiO₂ to reduce ultraviolet-induced damage, and the solar cells retained over 90% of their initial performance after 1000 hours of full sun illumination. Giordano *et al.*[18] demonstrated that Li-doped TiO₂ electrodes exhibit superior electronic properties, by reducing electronic trap states enabling faster electron transport. Guo *et al.*[19] proposed that a SnO₂:InCl₃ ETL was used in planar PSCs to simultaneously dope the ETL and passivate the defects at the ETL/perovskite interface, which expands the ETL/perovskite interface optimization work by using anions and cations for passivation and doping, respectively. Park[20] demonstrated that trap density in the MAPbI₃ close to TiO₂ was far lower than that without TiO₂, evidenced by the gate voltage-dependent threshold voltage difference based on the field effect transistor (FET) structure. Kim *et al.*[21] elucidated the atomistic

ᵃTianjin Key Laboratory of Optoelectronic Detection Technology and Systems, School of Electronic and Information Engineering, Tiangong University, Tianjin 300387, China. E-mail: liyuqiang@tiangong.edu.cn

ᵇKey Laboratory of Smart Grid of Ministry of Education, School of Electrical and Information Engineering, Tianjin University, Tianjin 300072, China

ᶜTianjin San'an Optoelectronics Co., LTD, Tianjin 300384, China

ᵈEngineering Research Center of High Power Solid State Lighting Application System of Ministry of Education, Tiangong University, Tianjin 300387, China

ᵉSchool of Physical Science and Technology, Tiangong University, Tianjin 300387, China

† Electronic supplementary information (ESI) available. See DOI: https://doi.org/10.1039/d2ra08143a

origin of efficient electron extraction and long stability of SnO$_2$ based PSCs through the analysis of band alignment, carrier injection, and interfacial defects in the SnO$_2$/MAPbI$_3$ interface using first-principles calculations at the Perdew–Burke–Ernzerhof (PBE0) + spin–orbit-coupling (SOC) + Tkatchenko–Scheffler (TS) dispersion-correction (PBE0-SOC-TS) level for all possible terminations and MA directions.

So far, most of the studies have focused on the enhancement of the electron mobility of SnO$_2$(TiO$_2$)/MAPbI$_3$ heterojunction interfaces by passivation and doping under ambient conditions and the interface oxygen vacancy induced by temperature and light. The electrical transport characteristics of SnO$_2$(TiO$_2$)/MAPbI$_3$ heterojunction interfaces under high pressure are rarely studied. High pressure has been proven to be a clean and powerful tool to analyze the physical properties of various heterojunction interfaces.[22,23] In this article, the electrical transport properties of SnO$_2$(TiO$_2$)/MAPbI$_3$ heterojunction interfaces are investigated from ambient to 20 GPa pressure by theoretical calculations, and the transport properties are investigated using physical parameters such as trap energy density, binding energy, charge transfer driving force and defects, and charge-capture rate. The electron transport abilities of SnO$_2$(TiO$_2$)/MAPbI$_3$ heterojunction interfaces are compared through the driving force of charge transfer, trap level density, and charge transfer defects calculations, using PDOS and differential charge density spectra under different pressures up to 20 GPa.

2. Theoretical basis and methods

We perform the noncollinear density functional theory (DFT) calculations with the hybrid PBE0 functional[24] including TS dispersion correction[25] using the Vienna *Ab initio* Simulation Package (VASP)[26] with dipole corrections. This is because the PBE0 functional can describe the band alignment of our system very well. In order to choose suitable exchange–correlations, we complete band gap calculation for SnO$_2$, TiO$_2$, and MAPbI$_3$ with different exchange–correlations using the PBE0-SOC-TS. We note that regardless of the exchange–correlation, the theoretical band gap is larger in TiO$_2$, whereas the experimental band gap is larger in SnO$_2$.[21] Therefore, instead of choosing different exchange–correlations for the SnO$_2$/MAPbI$_3$ and TiO$_2$/MAPbI$_3$ interfaces, we select only one potential for the whole interface calculations which can minimize the average band gap error. Since the PBE0-SOC-TS gives the minimum band gap error compared with the experimental band gap, we choose the PBE0-SOC-TS exchange–correlation. We uncover the mechanism behind the superior SnO$_2$- (TiO$_2$-)based PSCs by employing first-principles calculations using the PBE0-SOC-TS level for the SnO$_2$(TiO$_2$)/MAPbI$_3$ interface system owing to the lowest average band gap error. The projection augmented wave (PAW) method is used to carry out relevant calculations, using the Kohn–Sham (KS) equation based on density functional theory DFT,[27,28] a comparative study is performed on the ETL of SnO$_2$/
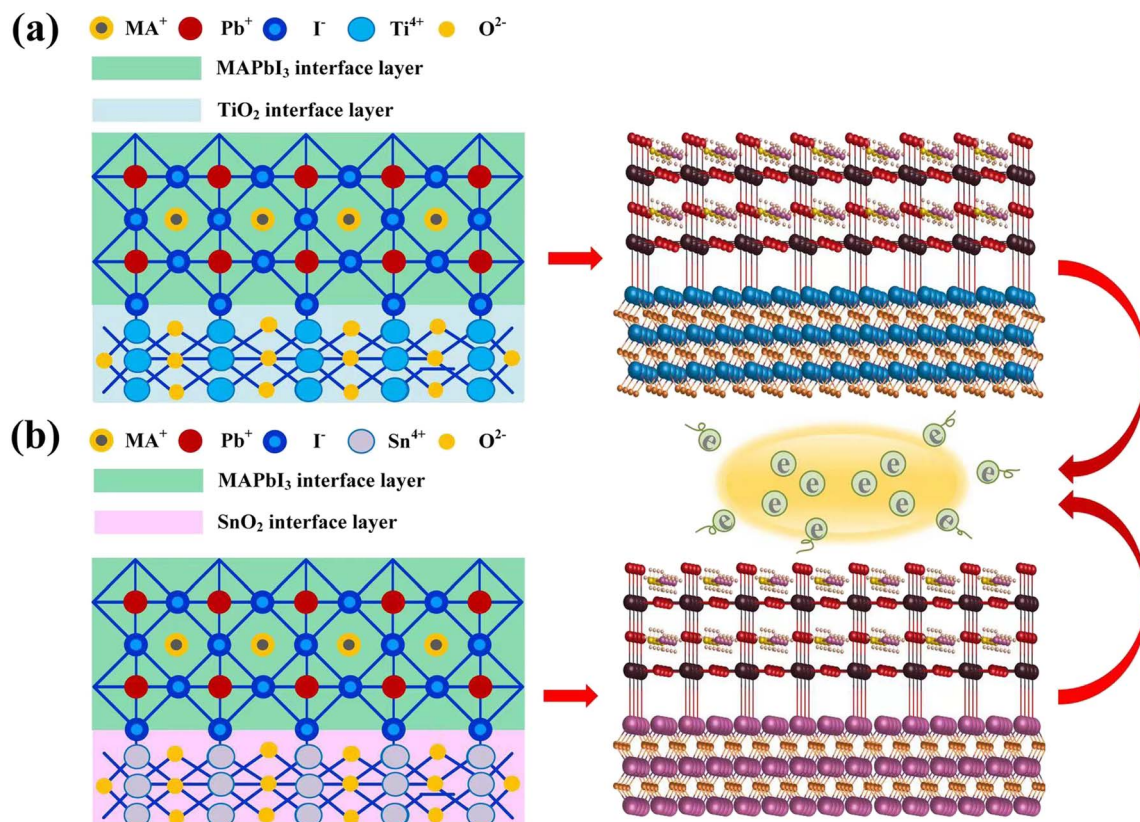

Fig. 1 Optimized models and structures of (a) TiO$_2$/MAPbI$_3$ heterojunction interface, (b) SnO$_2$/MAPbI$_3$ heterojunction interface, showing electron-capture mechanism similarly.

MAPbI$_3$ and TiO$_2$/MAPbI$_3$ heterojunction interfaces. Using the optimized SnO$_2$(TiO$_2$)/MAPbI$_3$ heterojunction interface modules, energy band, PDOS, and differential charge density spectrum are calculated from ambient pressure to 20 GPa.

Corresponding to the homologous electron-capture mechanism, the optimized models of the TiO$_2$/MAPbI$_3$ and SnO$_2$/MAPbI$_3$ heterojunction interfaces are shown in Fig. 1(a) and (b), respectively. The parameters of SnO$_2$(TiO$_2$)/MAPbI$_3$ heterojunction interface models are set (Table S3 in ESI†). The crystal cells on the surfaces of the [001], [011] and [111] plane SnO$_2$ and TiO$_2$, and [001] plane cubic MAPbI$_3$ are studied at 0 GPa, 5 GPa, 10 GPa, and 15 GPa. The slab consists of symmetric SnO$_2$ or TiO$_2$ (5 layers, 22 Sn/Ti atoms, and 44 O atoms) and MAPbI$_3$ [001], [011] and [111] (3 layers; MAI-termination: 4 MA molecules, 3 Pb atoms, and 10 I atoms; PbI$_2$-termination: 3 MA molecules, 4 Pb atoms, and 11 I atoms), where the lattice mismatches of SnO$_2$(TiO$_2$)/MAPbI$_3$ heterojunction interface models are as small as ~2.75% with a vacuum size of ~40 Å. Atomic coordinates of $\sqrt{2} \times \sqrt{2}$ supercells of SnO$_2$(TiO$_2$)/MAPbI$_3$ heterojunction interface models are shown in Tables S1 and S2 in the ESI.† Considering the lattice parameters of pristine SnO$_2$ ($\sqrt{2} \times \sqrt{2}$ supercell) and MAPbI$_3$ ($\sqrt{2} \times \sqrt{2}$ supercell) are about 6.55 and 6.25 Å, respectively, the average lattice parameter of 6.4 Å is selected which makes the lattice mismatch of both sides 2.75%. With combinations of MAI- and PbI$_2$-terminations with [001], [011], and [111] directions of MA in MAPbI$_3$, six types of SnO$_2$/MAPbI$_3$ (Fig. S2(a)–(c) in the ESI†) and TiO$_2$/MAPbI$_3$ (Fig. S2(d)–(f) in the ESI†) heterojunction interfaces are investigated under high pressure up to 20 GPa. Using the GCA-PBE functional, the truncation energy is set to 500 eV and the sampling density at point K is set to $3 \times 3 \times 5$. The convergence standard of structural optimization is that the difference in energy iteration is less than 1×10^{-6} eV per atom, the maximum force of atom is less than 0.02 eV Å^{-1}, and DFT+U is set. To reduce the lattice mismatch between MAPbI$_3$ and TiO$_2$ or SnO$_2$ in the DFT calculations, the initial distance between the four layers of atoms in the outermost layer of MAPbI$_3$ and TiO$_2$ or SnO$_2$ is set to 3.05 Å, and the vacuum layer at the heterojunction interface is set to 10.05 Å. Using the optimized TiO$_2$/MAPbI$_3$ and SnO$_2$/MAPbI$_3$ heterojunction interface models, the optimized Pb–I bond is relaxed from the original 3.15 Å to 3.45 Å, the length of the Ti–I bond and Sn–I bond is 3.38 Å, and the Pb–O bond is 2.35 Å. The area of the SnO$_2$(TiO$_2$)/MAPbI$_3$ heterojunction interface is selected to be about 1.68 nm^2. The optimized SnO$_2$/MAPbI$_3$ heterojunction interface shows stronger interface bonding and interface atom interaction.

3. Results and discussion

For the optimized SnO$_2$(TiO$_2$)/MAPbI$_3$ heterojunction interface modules, the interface binding energy of the two heterojunction interface models is:

$$\Delta E(\mathrm{SnO_2(TiO_2)/MAPbI_3}) = E(\mathrm{TiO_2})/E(\mathrm{SnO_2}) + E(\mathrm{MAPbI_3}) - E(\mathrm{SnO_2(TiO_2)/MAPbI_3}) \quad (1)$$

At the same time, the interface binding energy per unit area is:

$$\Delta E_{\mathrm{unit}}(\mathrm{SnO_2(TiO_2)/MAPbI_3}) = \frac{\Delta E(\mathrm{SnO_2(TiO_2)/MAPbI_3})}{S} \quad (2)$$

where $E(\mathrm{SnO_2})$, $E(\mathrm{TiO_2})$, and $E(\mathrm{MAPbI_3})$ respectively represent the energy of the SnO$_2$(TiO$_2$) and MAPbI$_3$ part before building
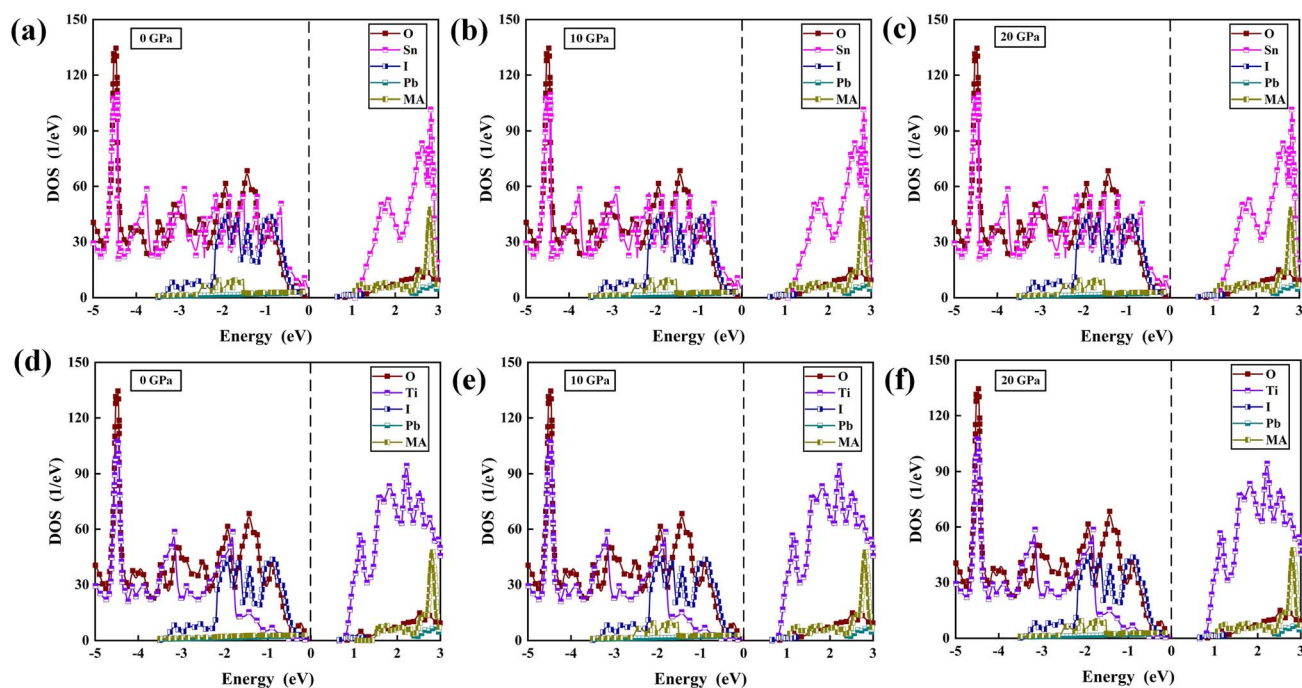

Fig. 2 PDOS of MA, Pb, I, Sn, O at (a) 0 GPa, (b) 10 GPa, (c) 20 GPa, and MA, Pb, I, Ti, O at (d) 0 GPa, (e) 10 GPa, (f) 20 GPa. Set Fermi energy level at 0 eV.

the SnO$_2$(TiO$_2$)/MAPbI$_3$ heterojunction interface models, E(SnO$_2$(TiO$_2$)/MAPbI$_3$) represents the overall energy of the SnO$_2$(TiO$_2$)/MAPbI$_3$ heterojunction interface models, and S represents that the selected interface area is about 1.68 nm^2. By comparing the binding energy values, we can quantify the relative stability of TiO$_2$/MAPbI$_3$ and SnO$_2$/MAPbI$_3$ heterojunction interface structures.

The MAPbI$_3$ model and SnO$_2$(TiO$_2$) models of SnO$_2$(TiO$_2$)/ MAPbI$_3$ heterojunction interfaces are optimized and calculated by static-self consistent calculations, and van der Waals force is introduced to correct them. The binding energy of SnO$_2$/MAPbI$_3$ [ΔE_{unit}(SnO$_2$/MAPbI$_3$) = −1.02 eV nm^{-2}] is significantly higher than the binding energy of TiO$_2$/MAPbI$_3$ [ΔE_{unit}(TiO$_2$/MAPbI$_3$) = −6.75 eV nm^{-2}] under ambient conditions (Table S4 in ESI†), which shows that the structure of the SnO$_2$/MAPbI$_3$ heterojunction interface is more stable. The SnO$_2$/MAPbI$_3$ heterojunction interface has higher interface binding energy, showing

stronger interface atom interactions and more stable heterojunction interface structure The difference in binding energy is smaller with applied pressure up to 20 GPa since the binding energy of the SnO$_2$/MAPbI$_3$ heterojunction interface increases less (Table S5 in ESI†). Compared with the TiO$_2$/MAPbI$_3$ heterojunction interface, the larger interfacial binding energy of the SnO$_2$/MAPbI$_3$ heterojunction interface roughly keeps the stable Pb–I bond leading to improvement in electrical transport properties.[29–31]

The PDOS of MA, Pb, I, Ti, Sn, and O in the TiO$_2$/MAPbI$_3$ and SnO$_2$/MAPbI$_3$ heterojunction interfaces are shown in Fig. 2(a)–(f) under different pressures, respectively. For the TiO$_2$/ MAPbI$_3$ heterojunction interface, the Fermi level is at the top of the valence band and the width of the band gap is about 0.75 eV. The bottom CBM (Conduction Band Minimum) of the conduction band of TiO$_2$ is basically composed of the valence electrons of Ti atoms, and the bottom CBM of MAPbI$_3$ is mainly
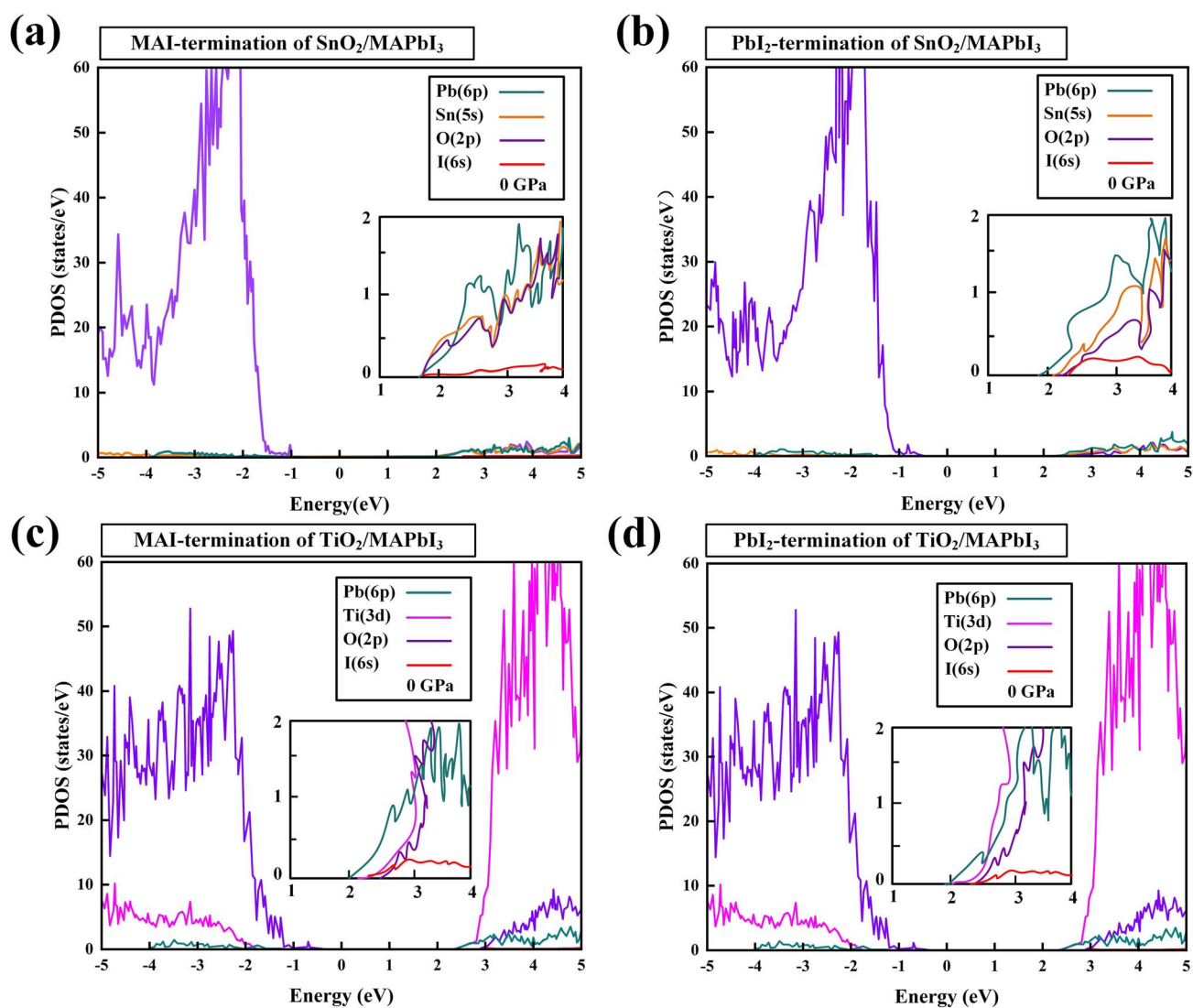

Fig. 3 PDOS of SnO$_2$/MAPbI$_3$ heterojunction interface: (a) MAI-termination and (b) PbI$_2$-termination. TiO$_2$/MAPbI$_3$ heterojunction interface: (c) MAI-termination and (d) PbI$_2$-termination. [Sn-5s orbital (orange), Ti-3d orbital (pink), O-2p orbital (purple), Pb-6p orbital (turquoise), and I-6s orbital (red)].

composed of the valence electrons of Pb atoms. Similarly, the VBM (Valance Band Maximum) at the left side of the Fermi level, that is, the valence band top of TiO$_2$, is mainly composed of the valence electrons of O atoms, and the VBM at the valence band top of MAPbI$_3$ is mainly composed of the valence electrons of I. The electronic DOS of MA atomic groups is far away from the Fermi level, and there are no peaks near the VBM and the CBM.[32,33] Most of the electron transport exists between the Pb–I framework and TiO$_2$, and MA atomic groups basically do not participate in the electron transport between the interfaces.[34–36] Ti forms a chemical bond with I in MAPbI$_3$, and electrons are transported from the surface of MAPbI$_3$ to TiO$_2$.[37–40] The Fermi energy level is at the top of the valence band, and the right side of the Fermi energy level, which is the bottom CBM of SnO$_2$, is basically composed of the valence electrons of Sn atoms, while the bottom CBM of MAPbI$_3$ is mainly the valence electrons of Pb atoms, as shown in Fig. 2(a)–(c). Similarly, the VBM of SnO$_2$ on the left side of the Fermi energy level is mainly composed of the valence electrons of O atoms, and the VBM of MAPbI$_3$ is mainly composed of the valence electrons of I. It is also analyzed that the electronic density of states of the MA atomic group is far away from the Fermi level, and there is no wave peak near the top of the VBM and the bottom of the CBM. Therefore, most of the electron transfer exists between the Pb–I skeleton and SnO$_2$, and the MA atomic group does not participate in the charge transfer between interfaces. Through the formation of a chemical bond between Sn and I in MAPbI$_3$, electrons are transferred from the MAPbI$_3$ surface to the SnO$_2$ surface. On the surface of Pb–I, the force of interface atoms is Pb–O atomic force. On the

right side of the Fermi energy level is the bottom CBM of TiO$_2$ which is basically composed of valence electrons of Ti atoms, and the bottom CBM of MAPbI$_3$ is mainly composed of valence electrons of Pb atoms, as shown in Fig. 2(d)–(f). Similarly, the top VBM of TiO$_2$ on the left side of the Fermi energy level is mainly composed of the valence electrons of O atoms, and the top VBM of MAPbI$_3$ is mainly composed of the valence electrons of I. The electronic state density of the MA atomic group is far away from the Fermi energy level, and there is no wave peak near the top VBM and the bottom CBM. Therefore, most of the electron transfer exists between the Pb–I skeleton and TiO$_2$. The MA atomic group does not participate in the charge transfer between interfaces. The electron transfers from the MAPbI$_3$ surface to the TiO$_2$ surface through the chemical bond formed between O and Pb in MAPbI$_3$. The charge transport driving force of TiO$_2$/MAPbI$_3$ heterostructure interfaces E_d(TiO$_2$/MAPbI$_3$) is:

$$\Delta E_d(\text{TiO}_2/\text{MAPbI}_3) = \text{CBM}(\text{MAPbI}_3) - \text{CBM}(\text{TiO}_2) \qquad (3)$$

On the Pb–I surface, the atomic force is displayed at the interface. The Fermi level is set at position 0, and the width of the band gap is about 0.45 eV.

For the SnO$_2$/MAPbI$_3$ heterojunction interface, the bottom CBM of the conduction band of SnO$_2$ is basically composed of the valence electrons of Sn atoms, and the bottom CBM of MAPbI$_3$ is mainly the valence electrons of Pb atoms.[41,42] The electronic DOS of the MA atomic group is also far away from the Fermi level, and no peak is observed near the VBM and CBM. Most of the electron transport exists between the Pb–I skeleton
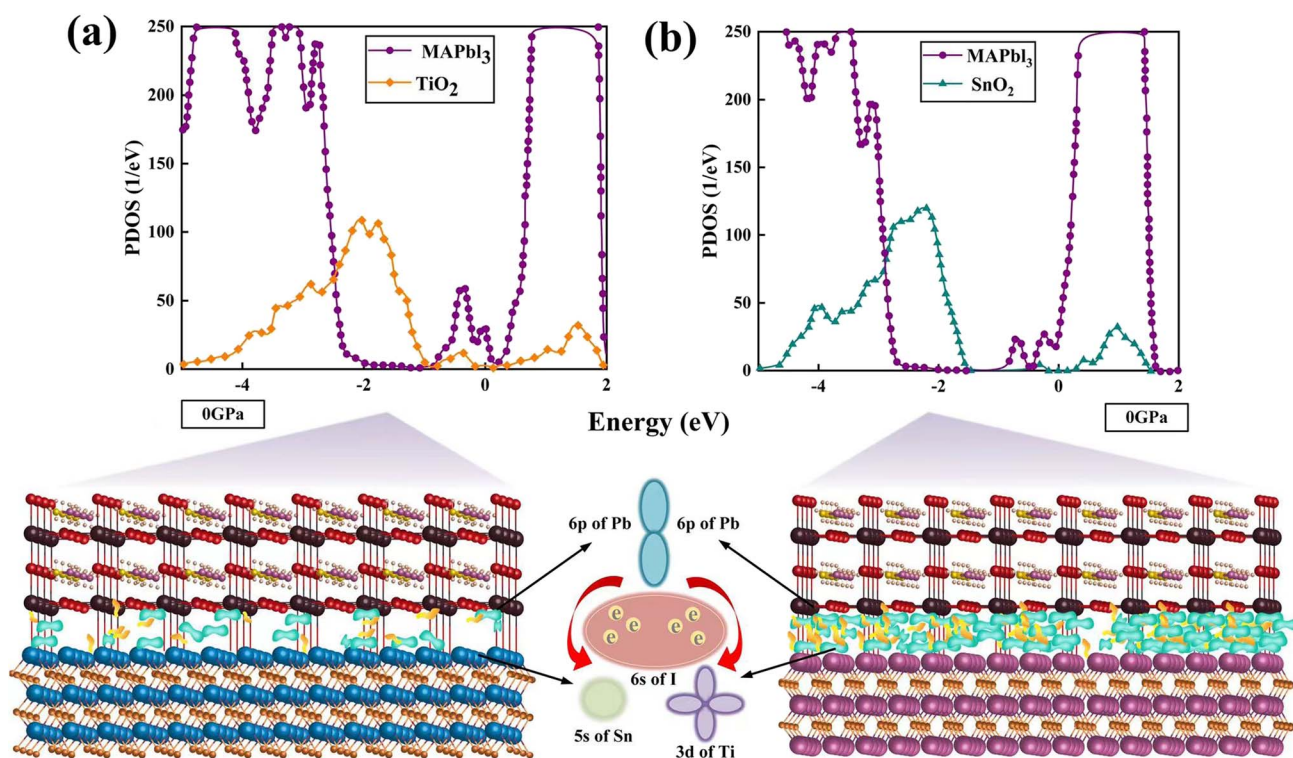

Fig. 4 PDOS of interface layer and differential charge density (a) on TiO$_2$/MAPbI$_3$, (b) on SnO$_2$/MAPbI$_3$ under ambient conditions. The yellow area represents gaining electrons, and the green area represents losing electrons.

and SnO$_2$, and the MA atomic group basically does not participate in the electron transport between heterostructure interfaces. Electrons are transported from the surface of MAPbI$_3$ to the surface of SnO$_2$ through the formation of a chemical bond between O and Pb in MAPbI$_3$.[43] The charge transport driving force of SnO$_2$/MAPbI$_3$ heterojunction interfaces E_d(SnO$_2$/MAPbI$_3$) is:

$$\Delta E_d(SnO_2/MAPbI_3) = CBM(MAPbI_3) - CBM(SnO_2) \qquad (4)$$

ΔE_d(SnO$_2$/MAPbI$_3$) is around 1.45 eV, while ΔE_d(TiO$_2$/MAPbI$_3$) is about 0.75 eV. Since 1.45 eV > 0.75 eV, the SnO$_2$/MAPbI$_3$ heterojunction interface has stronger charge transfer driving ability, showing superior electrical transport properties under ambient conditions. In order to study the electrical transport properties of SnO$_2$(TiO$_2$)/MAPbI$_3$ heterojunction interfaces under compression conditions, E_d(SnO$_2$(TiO$_2$)/MAPbI$_3$) and ΔE_d(SnO$_2$(TiO$_2$)/MAPbI$_3$) are obtained from ambient pressure to 20 GPa (Table S6 in the ESI†). It can be clearly seen that with the

increase in the applied pressure to 20 GPa, the larger ΔE_d between the charge transfer driving forces of SnO$_2$/MAPbI$_3$ and TiO$_2$/MAPbI$_3$ heterojunction interfaces reflects a more obvious difference in electrical transport properties. Note that the SnO$_2$/MAPbI$_3$ heterojunction interface shows a greater pressure dependence for the electrical transport properties than the TiO$_2$/MAPbI$_3$ heterojunction interface.

The PDOS of SnO$_2$/MAPbI$_3$ and TiO$_2$/MAPbI$_3$ heterojunction interfaces in MAI-termination and PbI$_2$-termination are shown in Fig. 3(a)–(d). The CBMs of SnO$_2$, TiO$_2$, and MAPbI$_3$ are mostly composed of Sn-5s, Ti-3d, and Pb-6p, respectively. The CBM orbital hybridizations occur between Sn-5s and Pb-6p orbitals at the SnO$_2$/MAPbI$_3$ interface and between Ti-3d and Pb-6p at the TiO$_2$/MAPbI$_3$ interface. The binding energies on the MA orientations of [001], [011] and [111] of MAI-termination and PbI$_2$-termination SnO$_2$/MAPbI$_3$ and TiO$_2$/MAPbI$_3$ are obtained (Tables S7–S10 in ESI†).

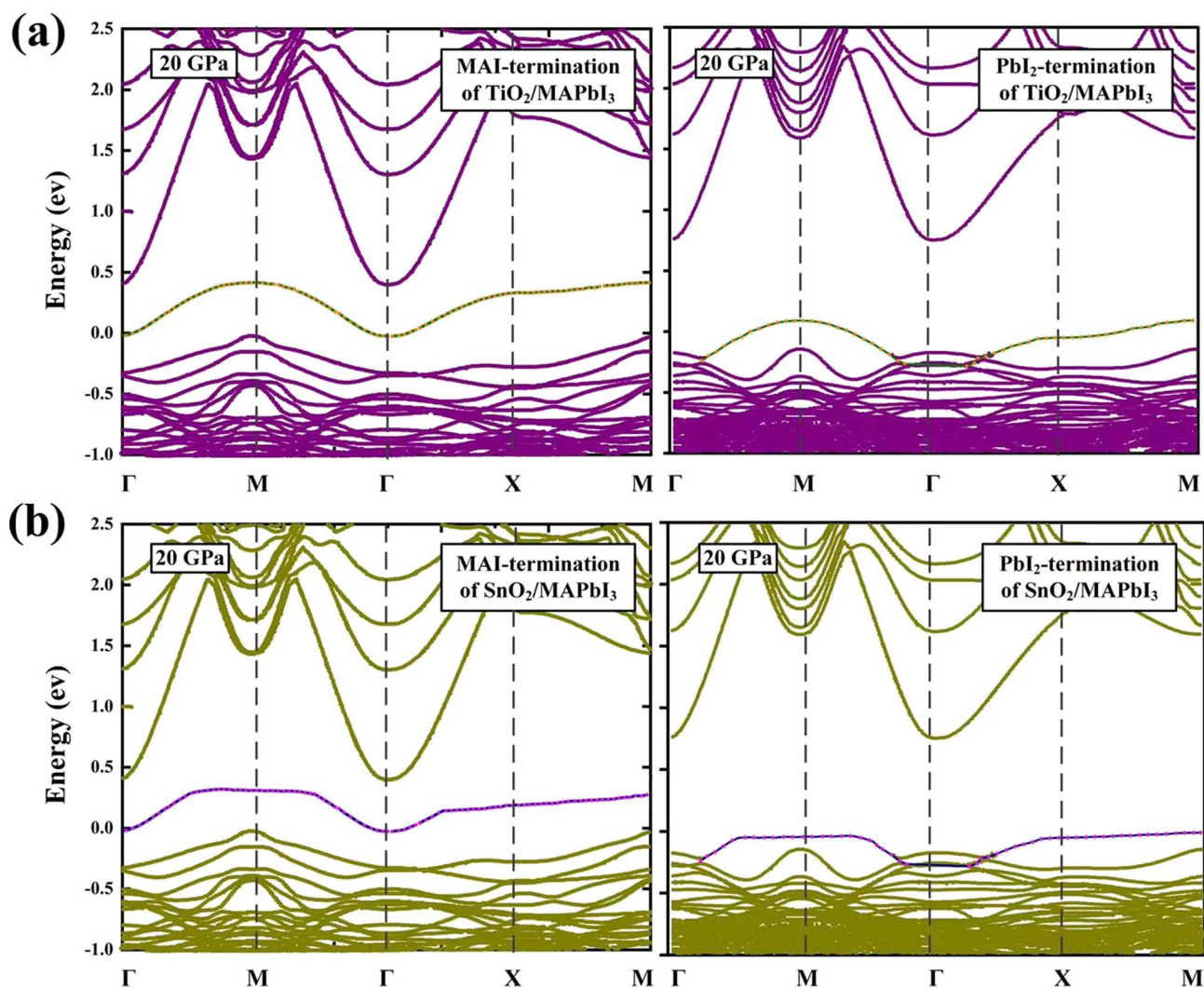The binding energy of the PbI$_2$-termination of the SnO$_2$/MAPbI$_3$ heterojunction interface is greater than that of MAI-

Fig. 5   Band structures of TiO$_2$/MAPbI$_3$ and SnO$_2$/MAPbI$_3$ heterojunction interfaces: (a) MAI-termination and PbI$_2$-termination, (b) MAI-termination and PbI$_2$-termination at 20 GPa. The pink and blue alternative circles and the orange and green alternative circles indicate the contribution of the surface Sn-5s states and Ti-5s states, respectively.

termination under different pressures, showing in the orbital hybridization of Pb ($MAPbI_3$) and Sn (SnO_2) interface atoms at the PbI_2-termination, which is conducive to efficient electron extraction. The orbital hybridization in the SnO_2/$MAPbI_3$ heterojunction interface is greater than that in TiO_2/$MAPbI_3$ owing to that the d orbital does not strongly hybridize with the s orbital or p orbital generally.[44,45] We note that the orbital hybridization difference is closely related to the carrier injection performance of the SnO_2(TiO_2)/$MAPbI_3$ heterostructure interfaces, showing that the SnO_2/$MAPbI_3$ heterojunction interface has better carrier injection due to the greater orbital hybridization compared with that at the TiO_2/$MAPbI_3$ heterojunction interface.[21]

The DOS of the SnO_2(TiO_2)/$MAPbI_3$ heterojunction interfaces are calculated to verify the SnO_2/$MAPbI_3$ heterojunction interface effectively reduces the trap energy level compared with the TiO_2/$MAPbI_3$ heterojunction interface under ambient conditions, as shown in Fig. 4(a) and (b). The trap energy levels in the interface band gaps of SnO_2/$MAPbI_3$ and TiO_2/$MAPbI_3$ heterojunction interfaces are used as the carrier binding center in the process of interface charge transfer.[46] The trap density is approximately 23.4% lower than that of the TiO_2/$MAPbI_3$ heterojunction interface, attributed to the trap energy level only existing in SnO_2 for the SnO_2/$MAPbI_3$ heterojunction interface. The SnO_2/$MAPbI_3$ heterojunction interface effectively reduces the defects affecting interface charge transfer and the trap energy level to reduce carrier recombination, which almost eliminates the interface defects caused by interface action in perovskites. The electron-capture rate of the TiO_2/$MAPbI_3$ heterojunction interface is approximately 27.5% more than that of SnO_2/$MAPbI_3$. Compared with the TiO_2/$MAPbI_3$ heterojunction interface, the SnO_2/$MAPbI_3$ heterostructure interface is less prone to capture electrons.

The band structures of the TiO_2/$MAPbI_3$ and SnO_2/$MAPbI_3$ heterojunction interfaces with Vo_0 are shown in Fig. 5(a) and (b) at 20 GPa. Corresponding to the PDOS of Fig. 4(a) and (b), the zero of energy represents the top of the valence band for the MAI-termination and PbI_2-termination of the TiO_2/$MAPbI_3$ and SnO_2/$MAPbI_3$ heterojunction interfaces. The green and orange alternative circles indicate the contribution of the surface Ti-5s states. The surface becomes a TiO-like environment attributed to the Vo_0 which makes the Ti-5s state almost filled with electrons.[47] For the MAI-termination and PbI_2-termination of SnO_2/$MAPbI_3$, the contribution of the surface Sn-5s states is shown by the pink and blue alternative circles. The surface becomes a SnO-like environment due to the Vo_0 filling the Sn-5s state with electrons. The SnO-like environment has better electron filling density, showing a superior electron transport environment compared with the TiO-like environment. The electron concentration difference in the SnO-like environment will be greater, which will result in greater electron transport ability compared with the TiO-like environment.

4. Conclusions

The SnO_2/$MAPbI_3$ heterojunction interface shows superior electrical transport properties compared with the TiO_2/$MAPbI_3$

heterostructure interface up to 20 GPa, manifested in the density of trap energy levels, binding energy, charge transfer driving force and defects, and charge-capture rate. The trap energy level of SnO_2/$MAPbI_3$ only exists in SnO_2, and the density of the trap energy level (23.4%) is much lower. The charge transfer driving force of the SnO_2/$MAPbI_3$ heterojunction interface (1.45 eV) is greater than that of TiO_2/$MAPbI_3$ (0.75 eV). The binding energy (-1.02 eV nm^{-2}) of the SnO_2/$MAPbI_3$ heterojunction interface is significantly higher than that of TiO_2/$MAPbI_3$ (-6.75 eV nm^{-2}), showing the obviously more stable SnO_2-based heterojunction structure. The electron-capture rate of the TiO_2/$MAPbI_3$ heterojunction interface is approximately 27.5% more than that of SnO_2/$MAPbI_3$. Compared with the TiO_2/$MAPbI_3$ heterojunction interface, the SnO_2/$MAPbI_3$ heterostructure interface is less prone to capture electrons, which is shown by the greater electron concentration difference in the SnO-like environment attributed to Vo_0 compared with the TiO-like environment.

Conflicts of interest

There are no conflicts to declare.

Acknowledgements

References

1 B. O'Regan and M. Grätzel, *Nature*, 1991, **353**, 737–740.

2 A. L. Linsebigler, G. Lu and J. T. Yates, *Chem. Rev.*, 1995, **95**, 735–758.

3 U. Bach, D. Lupo, P. Comte, J. E. Moser, F. Weissörtel, J. Salbeck, H. Spreitzer and M. Grätzel, *Nature*, 1998, **395**, 583–585.

4 E. Mosconi, E. Ronca and F. D. Angelis, *J. Phys. Chem. Lett.*, 2014, **5**, 2619–2625.

5 J. Jeng, Y. Chiang, M. Lee, S. Peng, T. Guo, P. Chen and T. Wen, *Adv. Mater.*, 2013, **25**, 3727–3732.

6 J. H. Heo, S. H. Im, J. H. Noh, T. N. Mandal, C. S. Lim, J. A. Chang, Y. H. Lee, H. J. Kim, A. Sarkar, M. K. Nazeeruddin, M. Gratzel and S. I. Seok, *Nat. Photonics*, 2013, **7**, 486–491.

7 J. Haruyama, K. Sodeyama, I. Hamada, L. Han and Y. Tateyama, *J. Phys. Chem. Lett.*, 2017, **8**, 5840–5847.

8 K. C. Ko, S. T. Bromley, J. Y. Lee and F. Illas, *J. Phys. Chem. Lett.*, 2017, **8**, 5593–5598.

9 J. Jeon, T. Eom, E. Lee, S. Kim, S. Kim, K.-H. Hong and H. Kim, *J. Phys. Chem. C*, 2017, **121**, 9508–9515.

10 C. Motta, F. E. Mellouhi, S. Kais, N. Tabet, F. Alharbi and S. Sanvito, *Nat. Commun.*, 2015, **6**, 7026.

11 F. Zheng, L. Z. Tan, S. Liu and A. M. Rappe, *Nano Lett.*, 2015, **15**, 7794–7800.

12 C. W. Myung, S. Javaid, K. S. Kim and G. Lee, *ACS Energy Lett.*, 2018, **3**, 1294–1300.

13 F. D. Angelis, D. Meggiolaro, E. Mosconi, A. Petrozza, M. K. Nazeeruddin and H. J. Snaith, *ACS Energy Lett.*, 2017, **2**, 857–861.

14 K. Oh, K. Jung, J. Shin, S. Ko and M.-J. Lee, *J. Mater. Sci. Technol.*, 2021, **92**, 171–177.

15 T. Leijtens, G. E. Eperon, S. Pathak, A. Abate, M. M. Lee and H. J. Snaith, *Nat. Commun.*, 2013, **4**, 2885.

16 D. Yang, X. Zhou, R. Yang, Z. Yang, W. Yu, X. Wang, C. Li, S. F. Liu and R. Chang, *Energy Environ. Sci.*, 2016, **9**, 3071–3078.

17 S. S. Shin, E. J. Yeom, W. S. Yang, S. Hur, M. G. Kim, J. Im, J. Seo, J. H. Noh and S. I. Seok, *Science*, 2017, **356**, 167–171.

18 F. Giordano, A. Abate, J. P. C. Baena, M. Saliba, T. Matsui, S. H. Im, S. M. Zakeeruddin, M. K. Nazeeruddin, A. Hagfeldt and M. Graetzel, *Nat. Commun.*, 2016, **7**, 10379.

19 X. Guo, J. Du, Z. Lin, J. Su, L. Feng, J. Zhang, Y. Hao and J. Chang, *Chem. Eng. J.*, 2021, **407**, 127997.

20 B. Park, *Results Phys.*, 2021, **23**, 104025.

21 J. Kim, K. S. Kim and C. W. Myung, *npj Comput. Mater.*, 2020, **6**, 100.

22 Y. Chen, Y. He, J. Wang, M. Li, M. Yu, R. Ye, B. Geng, Z. Yang, X. Zeng and J. Hu, *J. Phys. Chem. Lett.*, 2021, **12**, 989–996.

23 Y. Li, J. K. Cooper, R. Buonsanti, C. Giannini, Y. Liu, F. M. Toma and I. D. Sharp, *J. Phys. Chem. Lett.*, 2015, **6**, 493–499.

24 J. P. Perdew, K. Burke and M. Ernzerhof, *Phys. Rev. Lett.*, 1996, **77**, 3865.

25 A. Tkatchenko and M. Scheffler, *Phys. Rev. Lett.*, 2009, **102**, 073005.

26 G. Kresse and J. Furthmuller, *Comput. Mater. Sci.*, 1996, **6**, 15.

27 Y. Guo, Y. Xue and L. Xu, *Comput. Mater. Sci.*, 2021, **187**, 110081.

28 L. Wang, F. Si, F. Tang and H. Xue, *Mater. Res. Express*, 2019, **6**, 026312.

29 R. A. Kerner and B. P. Rand, *J. Phys. Chem. Lett.*, 2017, **8**, 2298–2303.

30 S. Ito, S. Tanaka and H. Nishino, *J. Phys. Chem. Lett.*, 2015, **6**, 881–886.

31 F. Zheng, L. Z. Tan, S. Liu and A. M. Rappe, *Nano Lett.*, 2015, **15**, 7794–7800.

32 F. Zhang, S. Y. Park, C. Yao, H. Lu, S. P. Dunfield, C. Xiao, S. Uličná, X. Zhao, L. D. Hill, X. Chen, X. Wang, L. E. Mundt, K. H. Stone, L. T. Schelhas, G. Teeter, S. Parkin, E. L. Ratcliff, Y.-L. Loo, J. J. Berry, M. C. Beard, Y. Yan, B. W. Larson and K. Zhu, *Science*, 2022, **375**, 71–76.

33 D. Liu and T. L. Kelly, *Nat. Photonics*, 2014, **8**, 133–138.

34 S. Zhang, J. Su, J. Zhang, Z. Lin, H. Yuan, J. Chang and Y. Hao, *J. Phys. Chem. Lett.*, 2021, **12**, 11834–11842.

35 E. P. Mukhokosi and M. Maaza, *J. Mater. Sci.*, 2022, **57**, 1555–1580.

36 J. M. Azpiroz, E. Mosconi, J. Bisquert and F. D. Angelis, *Energy Environ. Sci.*, 2015, **8**, 2118.

37 W. Shi and H. Ye, *J. Phys. Chem. Lett.*, 2021, **12**, 4052–4058.

38 K. Yan, Z. Wei, T. Zhang, X. Zheng, M. Long, Z. Chen, W. Xie, T. Zhang, Y. Zhao and J. Xu, *Adv. Funct. Mater.*, 2016, **26**, 8545–8554.

39 J. Zhang, K. Wang, Q. Yao, Y. Yuan, J. Ding, W. Zhang, H. Sun, C. Shang, C. Li, T. Zhou and S. Pang, *ACS Appl. Mater. Interfaces*, 2021, **13**, 29827–29834.

40 C. Yang, P. Du, Z. Dai, H. Li, X. Yang and Q. Chen, *ACS Appl. Mater. Interfaces*, 2019, **11**, 14044–14050.

41 T. Liu, L. Liu, M. Hu, Y. Yang, L. Zhang, A. Mei and H. Han, *J. Power Sources*, 2015, **293**, 533–538.

42 J. Yan, Z. Lin, Q. Cai, X. Wen and C. Mu, Choline chloride-modified SnO_2 achieving high output voltage in $MAPbI_3$ perovskite solar cells, *ACS Appl. Energy Mater.*, 2020, **3**, 3504–3511.

43 J. H. Heo and S. H. Im, *Nanoscale*, 2016, **8**, 2554–2560.

44 C. Li, J. Hu, S. Wang, J. Ren, B. Chen, T. Pan, X. Niu and F. Hao, *J. Phys. Chem. Lett.*, 2021, **12**, 4569–4575.

45 Y. Ai, Y. Zhang, J. Song, T. Kong, Y. Li, H. Xie and D. Bi, *J. Phys. Chem. Lett.*, 2021, **12**, 10567–10573.

46 G. S. H. Thien, N. A. Talika, B. K. Yap, H. Nakajima, S. Tunmee, N. Chanlek and B. T. Goh, *Ceram. Int.*, 2020, **46**, 29041–29051.

47 T. Bu, J. Li, F. Zheng, W. Chen, X. Wen, Z. Ku, Y. Peng, J. Zhong, Y. Cheng and F. Huang, *Nat. Commun.*, 2018, **9**, 4609.